

Neural Implicit Surface Reconstruction of Freehand 3D Ultrasound Volume with Geometric Constraints

Hongbo Chen^{a,b,c}, Logiraj Kumaralingam^d, Shuhang Zhang^a, Sheng Song^a, Fayi Zhang^a, Haibin Zhang^a, Thanh-Tu Pham^{d,e}, Kumaradevan Punithakumar^d, Edmond H. M. Lou^{d,e}, Yuyao, Zhang^a, Lawrence H. Le^{d,e,*}, Rui Zheng^{a,f,*}

^a*School of Information Science and Technology, ShanghaiTech University, Shanghai, 201210, China*

^b*Shanghai Advanced Research Institute, Chinese Academy of Sciences, Shanghai, 200050, China*

^c*University of Chinese Academy of Sciences, Beijing, 100049, China*

^d*Department of Radiology and Diagnostic Imaging, University of Alberta, Edmonton, T6G 2V2, Alberta, Canada*

^e*Department of Biomedical Engineering, University of Alberta, Edmonton, T6G 2V2, Alberta, Canada*

^f*Shanghai Engineering Research Center of Intelligent Vision and Imaging, ShanghaiTech University, Shanghai, 201210, China*

Abstract

Three-dimensional (3D) freehand ultrasound (US) is a widely used imaging modality that allows non-invasive imaging of medical anatomy without radiation exposure. Surface reconstruction of US volume is vital to acquire the accurate anatomical structures needed for modeling, registration, and visualization. However, traditional methods cannot produce a high-quality surface due to image noise. Despite improvements in smoothness, continuity, and resolution from deep learning approaches, research on surface reconstruction in freehand 3D US is still limited. This study introduces FUNSR, a self-supervised neural implicit surface reconstruction method to learn signed distance functions (SDFs) from US volumes. In particular, FUNSR iteratively learns the SDFs by moving the 3D queries sampled around volumetric point clouds to approximate the surface, guided by two novel geometric constraints: sign consistency constraint and on-surface constraint with adversarial learning. Our approach has been thoroughly evaluated across four datasets to demonstrate its adaptability to various anatomical structures, including a hip phantom dataset, two vascular datasets and one publicly available prostate dataset. We also show that smooth and continuous representations greatly enhance the visual appearance of US data. Furthermore, we highlight the potential of our method to improve segmentation performance, and its robustness to noise distribution and motion perturbation.

Keywords: Freehand 3D ultrasound, Self-supervised surface reconstruction, Implicit neural representation, Signed distance function

1. Introduction

Ultrasound (US) is a widely used imaging modality for clinical diagnosis, monitoring and analysis due to its low cost, radiation-free and real-time performance. The 3D

US with rich anatomical structure has been greatly developed and applied in many areas, such as 3D carotid artery diagnoses, automatic segmentation and organ visualization (Jiang and Chiu, 2023; Liu et al., 2019; Namburete et al., 2023). The data acquisition of 3D US imaging can be divided into 2D array, mechanical control, freehand scan without tracking sensor and freehand scan with tracking sensors (Prager et al., 2010; Prevost et al., 2018;

*Corresponding author

Email addresses: lawrence.le@ualberta.ca (Lawrence H. Le), zhengrui@shanghaitech.edu.cn (Rui Zheng)

Luo et al., 2022; Guo et al., 2022). Compared to the other three approaches, freehand 3D US with tracking sensors is a rapidly advancing technology to obtain the high-quality 3D volumes without limitation of field-of-view (Rohling et al., 1999; Mozaffari and Lee, 2017).

Freehand 3D US imaging technology commonly compounds the collected 2D B-mode images from transducer and the corresponding 3D poses from tracking device into a volume to reconstruct 3D internal structures of human body (Mozaffari and Lee, 2017). After reconstruction, volume rendering technique is usually adopted to transmit the 3D information in a translucent way or implicit neural representation (Li et al., 2021; Song et al., 2022; Wysocki et al., 2023). However, such voxel-based visualization makes it hard to recover accurate geometries and continuous surface (Batlle et al., 2023). Since each voxel element in the volume is considered for the rendered view, this technique also requires expensive computation costs for training (Huang and Zeng, 2017; Song et al., 2022).

Surface reconstruction is an alternate method to facilitate the geometric evaluation, morphological assessment, anatomical structure visualization, and surgery guidance (Zhou and Jagadeesan, 2020; Yeung et al., 2021; Velikova et al., 2024; Meng et al., 2024). Traditional surface reconstruction methods for freehand 3D US, like Contour filtering and Marching Cubes, usually convert the voxel representation after volume reconstruction to triangles or polygons mesh according to the segmented boundary (Mohamed and Siang, 2019). The geometric connection between each voxel is established following successive slices or voxel intensity, also known as ISO-Surface (Treece et al., 1999). However, traditional methods have connectivity problems because of the reconstructed empty holes or noise in US volume, this will lead to a rough surface, which requires further post-processing, such as smoothing and interpolation for better reconstruction results (Zhang et al., 2004). The quality of generated surface is also limited by the original reconstructed volume and voxel resolution (Nguyen et al., 2015).

In recent years, there has been a growing interest in using deep learning (DL) methods for surface reconstruction from medical imaging data, as an alternative to traditional methods, to bring increased accuracy and speed, as well as the ability to handle more complex and heterogeneous data (Farshian et al., 2023). Among various approaches, implicit neural representation (INR) has re-

ceived substantial attention in recent few years and successfully applied in medical imaging and graphics (Molaei et al., 2023; Reed et al., 2023). INR typically parameterizes a 3D surface structure as neural implicit functions through a deep neural network, such as encoding the signed distance functions (SDFs) as Multi-Layer Perceptrons (MLP) (Park et al., 2019). Within this context, INR provides resolution-agnostic surface rendering and improved memory efficiency. After training, the 3D scene can be effectively represented by a straightforward MLP, with the flexibility to re-generate mesh at varying resolutions during the reference stage.

However, the application of INR to freehand 3D US for continuous surface reconstruction is still missing. There are two main challenges in 3D freehand US to achieve high-quality surface reconstruction using deep learning. 1) Only the boundary of target structure in 2D segmentation mask cannot accurately reflect actual smooth surface because of the low signal-to-noise ratio (SNR) and poor pixel connectivity in US images. Additionally, it's difficult to extract the exact border and normal of complex surface. 2) Different anatomical structures have different geometric priors, and, it's difficult to acquire enough ground truth volumes, templates or surface normal to supervise the training stage for 3D surface reconstruction.

In this study, in order to address these issues, we propose, FUNSR, an efficient end-to-end online learning model to predict the SDFs for implicit surface representation from freehand 3D US point clouds data. Instead of preprocessing and extracting segmentation boundary as surface point cloud, the whole segmentation masks and their locations are directly transformed into a 3D volumetric point cloud as the input. Our target is to use the neural network to overfit underlying geometric surface in point clouds as the continuous SDFs representation to avoid disturbance of noise. Specifically, a set of 3D query points is sampled around each point in point clouds, and fed into the network to learn SDFs between query points and point clouds using a self-supervised strategy (Baorui et al., 2021).

In summary, there are four primary contributions:

- To the best of our knowledge, this is the first attempt to introduce an online self-supervised learning strategy of neural implicit surface reconstruction for freehand 3D US volumetric point clouds. The proposed

method can learn 3D continuous and high-resolution structures from individual input subject without the need for additional ground truth training data or post-processing.

- We introduce two geometric constraints aimed at enhancing surface reconstruction accuracy.
 - 1) Sign consistency constraint which is designed to correct the predicted SDFs within volumetric point clouds. This constraint ensures the network maintains an accurate sign in the input mask.
 - 2) On-surface constraint in accordance with adversarial learning strategy which is adopted to dynamically optimize the predicted SDFs when approaching to zero-level-set surface.
- We conduct extensive experiments to assess the structural fidelity and computational efficiency of our approach using four distinct datasets acquired by different US imaging systems. These datasets encompass four types of anatomical structures: hip joint, common carotid artery, carotid artery bifurcation and prostate (public dataset). The results indicate that our approach is competitive with current methods.
- We demonstrate the robustness of our model against various categories of input noise, including network segmentation noise, randomly distributed outliers and unexpected motion perturbation during freehand operation. We also thoroughly conduct ablation studies to investigate the effects of introduced geometric constraints and two input point cloud modalities on the surface reconstruction. We show that directly using volumetric point cloud is more straightforward and produces higher reconstruction quality compared to surface point cloud.

2. Related works

2.1. Traditional surface reconstruction in 3D ultrasound

Traditional surface reconstruction methods in 3D US can be simply classified into direct extraction and indirect segmentation. Zhang et al. (2002, 2004) propose to directly extract the surface from freehand 3D US B-mode scan using ISO-Surface after approximating a radial basis function across the pixels in 2D transverse images.

Nguyen et al. (2015) first segments the contours of region of interest (ROI) from transverse B-mode images in the reconstructed US volume. The Bézier-spline function is then used to smooth and interpolate the contours to form a high-quality triangle mesh. Kerr et al. (2017) adopts a column-wise threshold method to segment the bony surface of each image as a point cloud from ultrasonic synthetic aperture images. Surface mesh is directly produced by the point clouds using a wrapping algorithm.

2.2. DL-based surface reconstruction in medical imaging

Recent advances in DL-based 3D surface reconstruction methods have shown the promising results in magnetic resonance image(MRI), computerized tomography(CT) and 3D echocardiography. Wang et al. (2021) extends the graph convolutional network (GCN) to learn mesh deformation parameters of the target CT organ from surrounding detectable-organ features. A target organ template is provided to receive the predicted deformation parameters. After combining convolutional neural network (CNN) and GCN, the network can reconstruct 3D liver surface from a single 2D radiograph (Nakao et al., 2021). Strategies for joint segmentation and surface reconstruction have been designed to facilitate end-to-end training, converting the input MRI or CT volume directly to output meshes (Gopinath et al., 2021; Wickramasinghe et al., 2020). Cortical surface reconstructions from brain MRI scans mainly focus on the development of deformable template-based geometric networks (Santa Cruz et al., 2022; Ma et al., 2023; Bongratz et al., 2024). For echocardiography, Laumer et al. (2023) proposes a weakly supervised auto-encoder model to generate a 4D shape mesh from sequences of 2D mesh videos.

2.3. Implicit neural representation

Neural volume reconstruction. Concept of INR has been widely applied in different medical imaging modalities for volume reconstruction, including MRI slice-to-volume reconstruction (Xu et al., 2023), CT limited-view reconstruction (Song et al., 2023), 3D US freehand (sensorless) volume reconstruction (Wysocki et al., 2023; Yeung et al., 2024; Gaits et al., 2024; Eid et al., 2024). In particular, Velikova et al. (2024) attempts to integrate the neural volume reconstruction (NVR) and a post-processing module to reconstruct the abdominal aorta sur-

face from robotic 3D US imaging. This method (NVR-Poisson) first extracts a dense point cloud from the neural reconstructed volume, then downsamples the point cloud and fits a convex hull to obtain surface point cloud and corresponding point normal. The mesh is finally obtained through Poisson surface reconstruction.

Neural surface reconstruction. Currently, the development of end-to-end learning of an SDF has emerged as a primary choice for neural implicit surface reconstruction (Zha et al., 2023; Batlle et al., 2023). Park et al. (2019) proposes DeepSDF to learn an SDF in continuous space with a latent code by given ground truth signed distance values. Baorui et al. (2021) further demonstrates the feasibility of SDFs to learn 3D shape from surface point clouds using a neural pull operation without extra ground truth signed distance values, point cloud normal or occupancy value. Cruz et al. (2021) introduces the INR to MRI cortical surface reconstruction for the points in a continuous brain template coordinate system. Inspired by DeepSDF, Sander et al. (2023) trains an auto-decoder architecture to complete the high-resolution 3D left ventricle shape from sparse views of cardiac MRI (CMRI). Furthermore, Wiesner et al. (2024) encodes the spatial domain with an additional temporal domain into network to learn the shape of living cells from microscopy. Alongside SDFs, a recent approach has explored representing high-resolution shape through learning implicit occupancy function (Mescheder et al., 2019) using the architecture of DeepSDF from sparse volumetric masks in CT and MRI scans (Amiranashvili et al., 2024). In contrast to this occupancy-focused work, our study aims to reconstruct geometric surface and simultaneously establish a signed distance field, enabling potential applications in surgical navigation and multi-view reconstruction (Driess et al., 2021).

3. Materials and Methods

3.1. Overview

Our proposed method consists of two primary components: volumetric point cloud & query points generation, and neural implicit surface reconstruction. In addition, two geometric constraints, including sign consistency constraint (SCC) and on-surface constraint with adversarial learning (OSC-ADL), are designed to ensure superior reconstruction quality.

As shown in Fig. 1, given a sequence of 2D transverse images with associated 3D freehand poses, the coordinates of 2D segmented masks are transformed into a 3D point cloud \mathbf{P} in tracking space. The query points \mathbf{Q} are then sampled around each point in \mathbf{P} as input of MLP network. The SDFs between \mathbf{Q} and underlying surface described by \mathbf{P} are then progressively learned via neural network, guided by geometric constraints in a self-supervised manner. The triangle mesh is ultimately produced by Marching Cube algorithm using the predicted SDFs (Lorensen and Cline, 1987).

3.2. Volumetric point cloud and query point generation

For freehand 3D US system (Chen et al., 2021), each 2D pixel \mathbf{v}_s in the segmented mask space is first transformed into tracking space to acquire the 3D position, $\mathbf{v}_t = M_t M_c \mathbf{v}_s$. Where, $\mathbf{v}_s = [x_s, y_s, 0, 1]^T$ and $\mathbf{v}_t = [x_t, y_t, z_t, 1]^T$ are in homogeneous coordinate representation. M_c and M_t are the 4×4 calibration and tracking matrices from imaging system.

These 3D points \mathbf{v}_t are then spatially discretized into voxel grids and downsampled to acquire the volumetric point cloud $\mathbf{P} = \{\mathbf{p}_i, i = 1, \dots, N\}$ for uniform density distribution and efficient memory usage (Zhao et al., 2021; Kerr et al., 2017). For each \mathbf{p}_i in \mathbf{P} , a set of 3D query points $\mathbf{Q} = \{\mathbf{q}_{ij}, j = 1, \dots, l\}$ are randomly sampled around it following Gaussian distribution $(0, \delta)$ (Baorui et al., 2021). Here, δ is selected as the Euclidean distance between \mathbf{p}_i and its k -th nearest neighbor, N and l are the total number of 3D point cloud and query points, respectively.

3.3. Neural implicit surface reconstruction

3.3.1. Self-supervised learning of SDFs from point clouds

The SDFs are an implicit continuous representation to describe 3D shape by dividing the surface as exterior (positive), on-surface (zero) and interior (negative) (Zha et al., 2023; Park et al., 2019). In this paper, we indicate the SDFs through learning signed distances between surface represented by point cloud \mathbf{P} and query points \mathbf{Q} :

$$SDF(\mathbf{q}_{ij}, \mathbf{p}_i) = \{s \in \mathbb{R} \mid \mathbf{q}_{ij} \in \mathbb{R}^3, \mathbf{p}_i \in \mathbb{R}^3\} \quad (1)$$

where $\mathbf{p}_i = [x_i, y_i, z_i]$ is the 3D point in volumetric point cloud, $\mathbf{q}_{ij} = [x_{ij}, y_{ij}, z_{ij}]$ is sampled query point around \mathbf{p}_i , and s is the predicted signed distance between $\mathbf{q}_{ij} \in \mathbf{Q}$ and

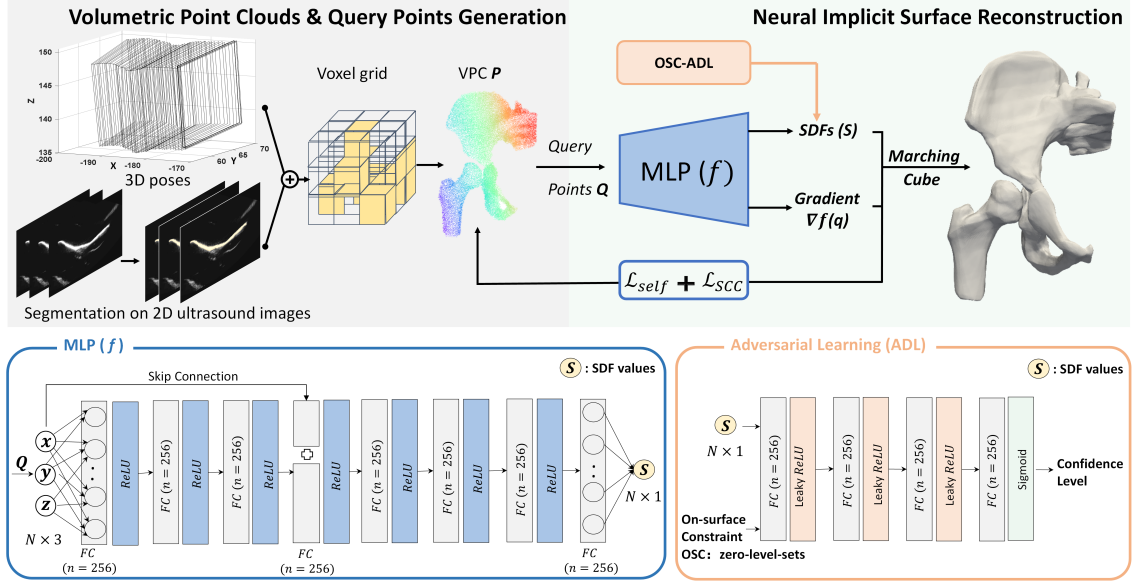


Figure 1: Overview of the proposed FUNSR, a neural implicit surface reconstruction method from freehand US volumetric point clouds (VPC). The VPC \mathbf{P} is first extracted from freehand 3D US volume after segmentation. A series of query points \mathbf{Q} are then sampled around each point in \mathbf{P} and fed into the neural network for learning of gradient ($\nabla f(q)$) via backpropagation and SDFs (s). The final mesh file is generated using Marching Cube algorithm using the predicted SDFs. Blue block at the bottom left depicts the MLP neural network with fully connected layers (FC), and orange block at the bottom right represents the on-surface constraint with adversarial learning (OSC-ADL).

surface represented by $\mathbf{p}_i \in \mathbf{P}$. The underlying surface boundary is depicted by a zero-level-set of $SDF(\mathbf{*}) = 0$, which can be easily used to extract mesh by Marching Cube.

To simplify the notation, each query point is re-denoted as $\{q_k, k = 1, \dots, l\}$. Then, for each q_k , we find its nearest neighbor point $t_k \in \mathbf{P}$ under the Euclidean distance for calculation of self-supervised loss. As described in Fig. 1, an MLP neural network f is trained to learn the SDF value and gradient of a given query point q_k in \mathbf{Q} . The query point is then projected along or against the learned gradient to its nearest point t_k using the predicted SDF value. This projection process is illustrated in Fig. 2 (a) and formulated as the below equation (Chou et al., 2022; Baorui et al., 2021),

$$q_k' = q_k - s \times \frac{\nabla f(q_k)}{\|\nabla f(q_k)\|_2} \quad (2)$$

where s , also denoted as $f(q_k)$, is the predicted SDFs of q_k from the MLP network, $\nabla f(q_k) / \|\nabla f(q_k)\|$ is the normalized gradient of network, indicating the direction in

3D space where signed distance increases most rapidly. Here, $\nabla f(q_k)$ is derived by backpropagation during the MLP training.

Following Neural-pull (Baorui et al., 2021), we minimize the self-supervised L2-distance loss to optimize the projected q_k' approaching its nearest neighbor $t_k \in \mathbf{P}$:

$$\mathcal{L}_{self} = \frac{1}{K} \sum_{k \in [1, K]} \|q_k' - t_k\|_2^2 \quad (3)$$

where K is the batch size during the training.

3.3.2. Sign consistency constraint for volumetric point clouds

In order to learn a better underlying surface, our input is the whole mask instead of boundary. However, as proved in (Chou et al., 2022), only using Eq. (3) to supervise training has no explicit penalties for the predicted wrong sign when query point is close to the point cloud. This limitation will cause the network to fail to converge to a stable status, especially inside the mask.

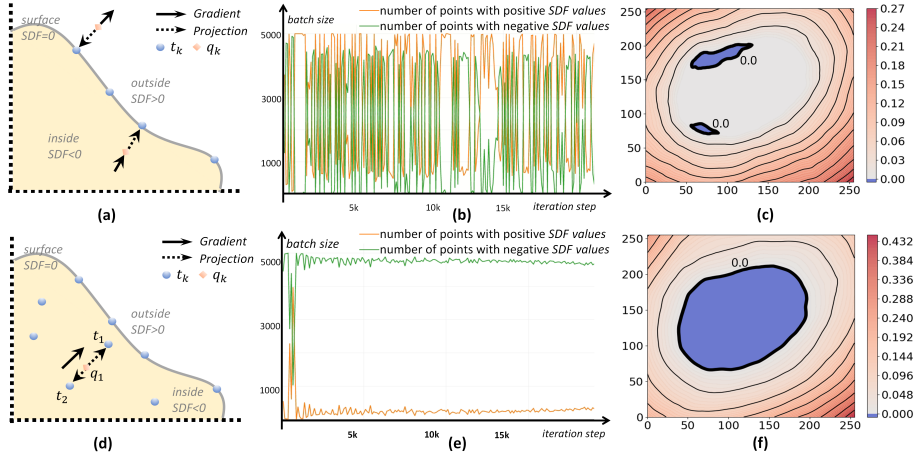


Figure 2: The 2D demonstration of sign consistency constraint from carotid sample. (a) and (d) Projection around the surface and inside surface. (b) and (e) Plot of the number of points with pos/neg SDF value learned from \mathcal{L}_{self} loss only and with SCC. (c) and (f) Level-sets of SDF learned from \mathcal{L}_{self} loss only and with SCC. The blue region and red region indicate the negative area (inside) and positive area (outside), respectively.

A simple 2D case is illustrated in Fig. 2 (d), t_1 and t_2 are two points inside the surface, q_1 is the corresponding nearest query point around t_1 and t_2 , respectively. Following Eq. 2, the network will predict a negative sign distance to project q_1 to t_1 along the direction of gradient and minimize loss Eq. (3). However, in next training batch, t_2 , as the opposite direction of t_1 , will make the network try to change the sign to minimize Eq. (3) against the gradient. Obviously, this will lead the predicted sign inside mask to be in a chaotic state. As shown the Fig. 2 (b) and (c), the number of positive signs and negative signs varies wildly at each iteration and the zeros-level-set boundary disappears.

To address this problem, we introduce a direction loss as \mathcal{L}_{SCC} to balance the distance loss by following formula,

$$\mathcal{L}_{SCC} = \frac{1}{K} \sum_{k \in [1, K]} 1 - \cos \left(\nabla f(q_k), \frac{(q'_k - t_k)}{\|q'_k - t_k\|_2} \right) \quad (4)$$

where $1 - \cos(*, *)$ is the cosine distance to penalize direction deviation between two non-zero vectors to the range of $\{0, 2\}$.

When distance loss \mathcal{L}_{self} converges near to surface boundary, the network may begin to oscillate. At this point, SCC constraint on the projection path starts to

guide the network to change direction of gradient in next training batch, but not the sign, thereby facilitating the model in learning correct SDFs. Fig. 2 (b) and (c) demonstrate that the predicted positive and negative values are quickly stabilized after using proposed SCC, and the zero-level-set boundary is still well-preserved for surface representation.

3.3.3. On-surface constraint with adversarial learning

On-surface prior is another important geometric constraint to improve the surface reconstruction. Ideally, the network will converge to actual surface boundary, allowing us to accurately distinguish the inside and outside of a structure by $SDF = 0$ on the surface. However, lacking on-surface prior can result in inaccurate or even wrong prediction in complex medical structures, such as the shapes with polygonal holes or noisy input.

Adversarial learning strategies have previously been investigated for point cloud reconstruction and 3D US sensorless reconstruction (Li et al., 2019; Luo et al., 2023). To leverage more information, we propose encoding the OSC-ADL to enforce network to learn a more accurate shape. The ADL module, consisting of four fully connected MLP and Leaky ReLU activation functions, serves as an adversarial discriminator \mathcal{D} for the reconstruction.

Specifically, the actual boundary corresponds to a prior SDF of 0, representing on-surface constraint, while the SDF learned from network is considered the 'fake' value. The predicted signed distance values from network f are fed into discriminator, and the confidence levels are generated using an attached sigmoid layer. This enables the model to penalize points that are close to zero-level sets but do not belong to the surface. Through this strategy, the network's SDF predictions are iteratively guided to accurately represent surface boundary of anatomical structures, ultimately enhancing the precision of our surface reconstruction methodology.

Overall, the entire network is optimized end-to-end by minimizing \mathcal{L}_G and \mathcal{L}_D in an adversarial manner during the training stage. The \mathcal{L}_G is adversarial generator loss to train MLP with \mathcal{L}_{self} and \mathcal{L}_{scc} , and \mathcal{L}_D is adversarial discriminator loss. Here, we directly minimize the least-squared adversarial loss (Mao et al., 2017) between predicted SDF values and zero scalar field's value:

$$\mathcal{L}_G = \lambda_{self} \mathcal{L}_{self} + \lambda_{scc} \mathcal{L}_{scc} + \lambda_G \frac{1}{2} [D(s) - 1]^2 \quad (5)$$

$$\mathcal{L}_D = \frac{1}{2} [D(s)^2 + (D(s') - 1)^2] \quad (6)$$

where, λ_{self} , λ_{scc} and λ_G are loss weights, $D(s)$ is the confidence value predicted by D from learned SDFs, G , D are optimized alternatively in the training process, s and s' denote the predicted signed distances and zero scalar field's value (on-surface constraint), respectively. The size of the zero scalar field's value is defined following batch size.

4. Experiments setup

4.1. Datasets

To assess the generalizability of our proposed method, four types of datasets are involved in this study. More comprehensive specifications of these datasets are listed in Appendix A.

- 1) Phantom dataset. Two anthropomorphic hip joint phantoms are scanned underwater by an operator using a portable freehand 3D US imaging system (Chen et al., 2020). A straightforward threshold

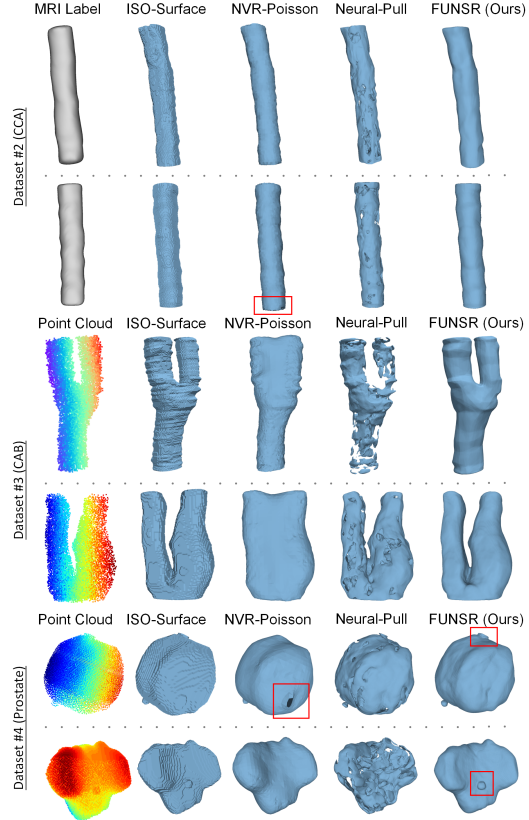


Figure 3: Six examples of reconstructed meshes from *in-vivo* datasets using four methods at 1.5×10^4 iterations. Blue-to-red color in point cloud indicates the directional changes from left to right and red boxes highlight the detailed differences between four methods.

method is utilized for image segmentation. The corresponding computer-aided designed (CAD) model of each hip phantom served as a reference.

- 2) Common carotid artery (CCA) dataset. This dataset comprises 10 shapes of left and right CCA collected from five volunteers. Annotations of carotid artery are derived from an experienced rater through manual labeling. Paired MRI scans for each volunteer are conducted for reference at MR Lab at School of Biomedical Engineering at ShanghaiTech University on a 3T uMR 890 MRI system (United Imaging Healthcare, Shanghai, China). The imaging resolution for CCA setting is 0.4 mm.

- 3) Carotid artery bifurcation (CAB) dataset. This dataset consists of 77 CAB shapes collected from the clinical setting. Approval for this study was granted by the relevant local research ethics committees. Reference annotations for all the images are determined through manual labeling. We further partition the datasets into a training set (57 cases) and a test set (20 cases) for automatic segmentation following (Zhang et al., 2023). The automatically segmented masks from test set are utilized for experimental analysis of segmented noisy inputs.
- 4) Prostate Dataset. This dataset includes 108 patients from MICCAI 2023 MRI to US Registration for Prostate (μ -RegPro) Challenge (Baum et al., 2023). The publicly available 73 transrectal ultrasound (TRUS) volumes have been divided by organizers into 65 for training and 8 for validation in registration task. These volumes contain well-defined anatomical landmarks for reference, including prostate gland, visible lesions and zonal structures etc¹. This dataset is employed to examine how our method can be directly applied to 3D US volume with masks.

4.2. Baseline methods

ISO-Surface. This is a classic algorithm in medical imaging graphics for surface reconstruction (Treece et al., 1999). We directly generate the surface mesh from segmented masks using ISO-Surface.

NVR-Poisson. Two stages are involved in this method for surface reconstruction of the abdominal aorta from robotic 3D US imaging (Velikova et al., 2024): a) semantic neural volume reconstruction (NVR) (Song et al., 2022) and b) surface point cloud extraction and downsampling based on the reconstructed volume and mesh generation using Poisson surface reconstruction from point cloud². For the implementation of stage a), we schedule the training of NVR for 100,000 iterations with a batch size of 200,000. Other hyperparameters are configured following (Song et al., 2022), and network architecture design is the same as (Mildenhall et al., 2020).

¹<https://muregpro.github.io/>

²https://www.open3d.org/docs/latest/tutorial/Advanced/surface_reconstruction.html

Neural-Pull. Our approach is established based on the self-supervised learning strategy that originally introduced in this method for computer vision applications (Baorui et al., 2021).

4.3. Evaluation metrics

Fidelity. Six accuracy metrics are employed to comprehensively access the reconstruction fidelity, including Dice similarity coefficient (DSC), Jaccard coefficient (intersection over union / IoU), Average Surface-to-Surface Distance (ASD), L2-Chamfer Distance (CD), Hausdorff Distance (HD) and 95% Hausdorff Distance (HD95). Here, DSC and IoU coefficients are specifically adopted to verify the area similarity between predicted closed surfaces and reference closed surfaces. The distance metrics quantify the boundary discrepancies between reconstructed surfaces and their references.

Geometry. We also geometrically evaluate the completeness and smoothness of reconstructed meshes from different methods. We choose topological measures (connected component (CC), genus (Popescu-Pampu, 2016; Martelli, 2022)) to assess the shape completeness, and Gaussian curvature computation as well as kernel density estimation (KDE) to assess the surface smoothness.

4.4. Implementation details

During the training phase, all extracted point clouds are randomly downsampled to $N = 20,000$ using farthest point sampling (FPS) and 25 query points are sampled for each point $p_i \in \mathbf{P}$. The distance between p_i and its 50-th nearest neighbor point ($k = 50$) is computed to determine σ in Section 3.2 for query points generation. We use geometric network initialization strategy (Atzmon and Lipman, 2020) to initialize the weights of MLP following (Baorui et al., 2021). The MLP network is initialized to approximate the signed distance function of an r -radius sphere before training. Here, r is set to 0.5 for the bias item of MLP network. The network is trained for 1.5×10^4 iterations using Adam optimizer with a learning rate of 0.001, a momentum of 0.9 and a batch size of 5000. All the segmented point clouds are normalized in a range of $\{-1, 1\}$. The λ_{self} is set as 1, and λ_{sc} , λ_{gan} are set as 0.005 to control the query points near to the surface, respectively. Our network is implemented using Pytorch and trained on a single NVIDIA RTX 3090 GPU with 24 GB memory.

Table 1: Mean (std) results of surface reconstruction performance on different methods from four types of datasets.

Dataset #1 (Phantom) Methods	CC	Genus	ASD(mm) ↓	CD(mm) ↓	HD(mm) ↓	HD95(mm) ↓
ISO-Surface	154 (200)	non-manifold	4.69 (3.41)	4.45 (3.22)	26.86 (11.48)	12.77(7.89)
NVR-Poisson	14 (13)	99 (125)	4.78 (2.27)	4.59 (1.87)	26.33 (9.92)	13.39 (4.72)
Neural-Pull	73 (68)	79 (69)	3.31(0.69)	2.78 (0.36)	3.43 (2.02)	1.75(0.18)
FUNSR(Ours)	2 (0)	1 (0)	1.51(0.36)	1.04 (0.01)	2.09 (1.59)	0.77(0.38)
Dataset #2 (CCA) ¹ Methods	DSC ↑	IoU ↑	ASD(mm) ↓	CD(mm) ↓	HD(mm) ↓	HD95(mm) ↓
ISO-Surface	0.848 (0.03)	0.737 (0.04)	0.60 (0.12)	0.60 (0.12)	2.18(0.17)	1.39 (0.29)
NVR-Poisson	0.850 (0.02)	0.739 (0.04)	0.60 (0.11)	0.60 (0.11)	2.36 (0.37)	1.36 (0.23)
Neural-Pull	0.662 (0.04)	0.496 (0.04)	0.64 (0.12)	1.03 (0.09)	3.99 (0.21)	1.48 (0.20)
FUNSR(Ours)	0.861 (0.02)	0.756 (0.04)	0.60 (0.10)	0.60 (0.10)	2.31 (0.46)	1.22 (0.27)
Dataset #3 (CAB) Methods	DSC ↑	IoU ↑	ASD(mm) ↓	CD(mm) ↓	HD(mm) ↓	HD95(mm) ↓
ISO-Surface	0.94 (0.02)	0.89 (0.04)	0.17 (0.03)	0.16 (0.03)	0.75 (0.43)	0.28 (0.10)
NVR-Poisson	0.82 (0.18)	0.72 (0.18)	0.62 (0.93)	0.64 (1.13)	4.04 (3.61)	2.05 (1.81)
Neural-Pull	0.70 (0.19)	0.56 (0.17)	0.43 (0.90)	1.09 (1.90)	4.54 (4.31)	0.96 (1.92)
FUNSR(Ours)	0.95 (0.05)	0.90 (0.06)	0.17 (0.11)	0.15 (0.11)	0.79 (0.62)	0.35 (0.08)
Dataset #4 (Prostate) Methods	DSC ↑	IoU ↑	ASD(mm) ↓	CD(mm) ↓	HD(mm) ↓	HD95(mm) ↓
ISO-Surface	0.72 (0.38)	0.68 (0.39)	0.74 (0.33)	0.75 (0.29)	3.10 (4.92)	1.34 (1.89)
<i>NVR-Poisson</i> ²	0.80 (0.34)	0.76 (0.35)	0.64 (0.09)	0.65 (0.15)	3.71 (2.15)	1.21 (0.40)
Neural-Pull	0.79 (0.05)	0.66 (0.07)	0.63 (0.04)	3.12 (0.13)	17.17 (0.77)	1.19 (0.08)
FUNSR(Ours)	0.97 (0.01)	0.94 (0.01)	0.59 (0.04)	0.55 (0.05)	1.53 (0.33)	1.08 (0.17)

¹ Three decimal places are used for DSC and IoU in Dataset #2 to facilitate more nuanced comparisons.² Only second stage of *NVR-Poisson* is involved since Dataset #4 already contains reconstructed 3D volume.

During the reference stage, we set a threshold of Marching Cube to 0 and resolution to $256 \times 256 \times 256$ to generate mesh based on the predicted SDFs (Park et al., 2019; Baorui et al., 2021; Wiesner et al., 2024). This resolution choice can achieve a balance between visualization appearance and reference speed according to the findings in Wiesner et al. (2024).

5. Experimental results

5.1. Surface reconstruction performance

We benchmark the structural fidelity of our results against three methods across all four datasets, using man-

ual labels as inputs. As detailed in Table 1, our method demonstrates continuous significant superiority over three methods on Datasets #1 and #4, and achieves similar performance with ISO-Surface on Dataset #3. Notably, we observe a substantial average decrease of 32% ASD, 68% in CD, 64% in HD, and 37% HD95 across all the datasets when compared with Neural-Pull, indicating the superior accuracy of proposed method in matching reconstructed surfaces on the respective references.

For Dataset #1 (phantom), we report topological measures to access the shape completeness rather than similarity coefficients, as US signal can not penetrate phantom surface to accurately capture the structure behind surface.

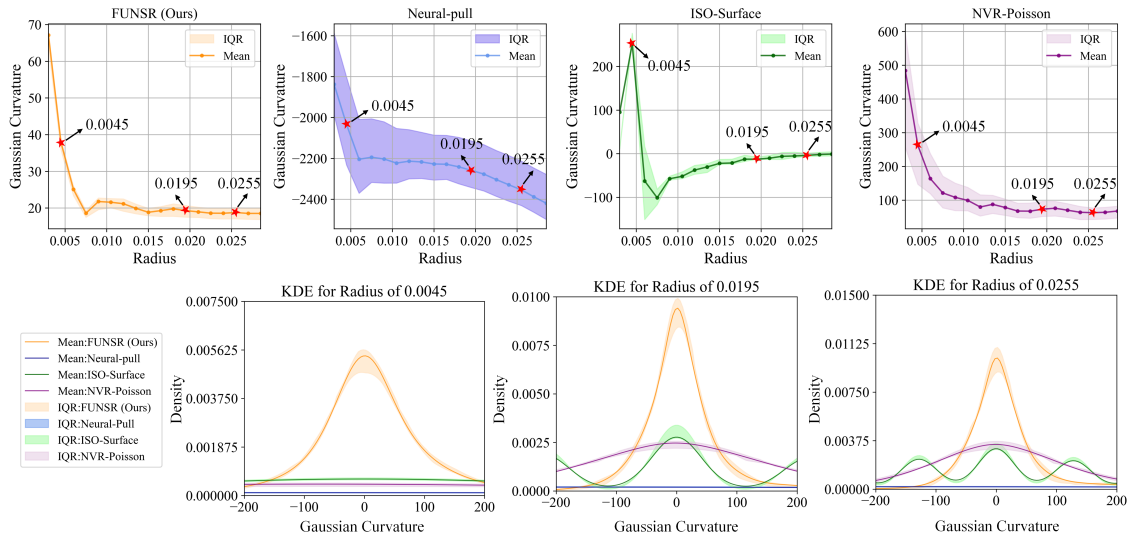


Figure 4: Quantitative evaluation of smoothness of reconstructed meshes from Dataset #2 (CCA). The plots show descriptive statistics (mean and interquartile range) of four methods based on Gaussian curvature (top) and kernel density estimation (KDE, bottom). For density of four methods, the higher amplitude of Gaussian curve, the smoother it is.

The topological analysis for CAD model only has two CC and one genus. However, as shown at the top of Table 1, three baseline methods fail to maintain the accurate shape integrity, particularly ISO-Surface, which results in a high number of CC (154 ± 200) and non-manifold shape for genus calculation. A possible explanation for this is that Dataset #1 contains noise and outliers introduced by threshold segmentation. The combined NVR and Poisson surface reconstruction (NVR-Poisson) method displays some improvements over ISO-Surface and Neural-Pull, yet the performance is limited. Our method (FUNSR) achieves 1.51 mm ASD and 1.04 mm CD, approaching the imaging resolution of the data acquisition system.

In Dataset #2 (CCA), no significant differences are observed in the results among ISO-Surface, NVR-Poisson, and our method when compared with MRI scans, due to the simplicity of vascular structures in this dataset for reconstruction. Similarly, ISO-Surface performs comparably to our method in Dataset #3 (CAB). However, NVR-Poisson struggles to reconstruct the bifurcation structure of carotid artery, leading to reduced performance in this dataset. FUNSR (Ours) demonstrates superior fidelity across the other three methods, except for HD and HD95

metrics. This exception can be attributed to our method’s ability to smooth out fluctuations in vascular shape caused by breathing during scans. Such a smoothing effect might prevent the reconstructed mesh from perfectly matching original input labels.

Dataset #4 (Prostate) vividly showcases the advantages of our approach, particularly its capability to accurately handle finer structures, such as tumors on the prostate gland surface (as shown in Fig. 3). In contrast, when ISO-Surface and NVR-Poisson attempt to process these surface details, they often create holes or lose details, leading to decreased DSC and IoU performance. A significant challenge for the second stage of NVR-Poisson is accurately estimating the correct point normal, which is essential for successful Poisson surface reconstruction on these datasets.

We qualitatively present six *in-vivo* examples of reconstructed meshes in Fig. 3. While ISO-Surface is capable of generating accurate shapes, it is constrained by the resolution and discontinuities. NVR-Poisson method leverages INR and Poisson to produce smooth and continuous shapes. However, this approach may over-smooth structures in complex cases, for instance, the carotid artery

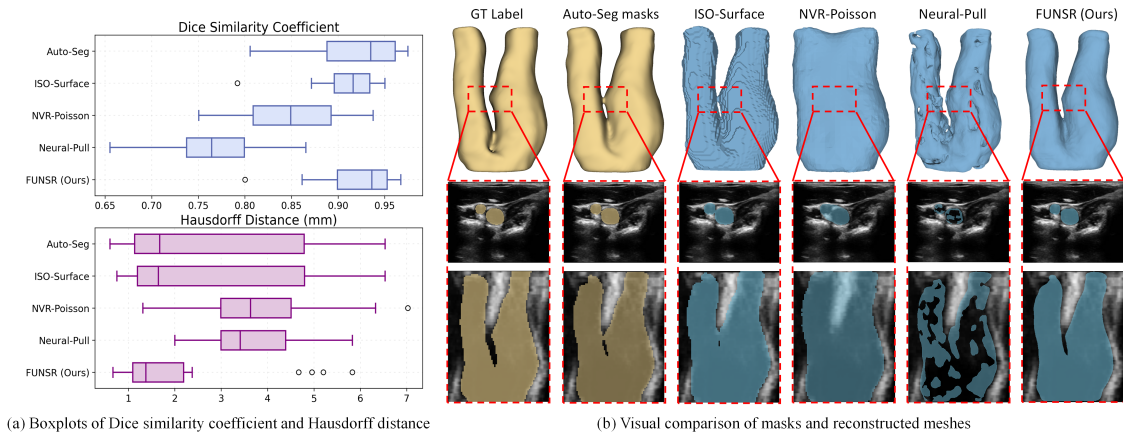


Figure 5: Quantitative and qualitative evaluation for Dataset #3 (CAB)-test. (a) Boxplots of Dice similarity coefficient and Hausdorff Distance from four methods and automatic network segmentation (Auto-Seg). (b) Visualization of ground truth (GT) label, Auto-Seg masks and reconstructed meshes from four methods in 3D space, 2D cross-section plane and 2D coronal plane.

Table 2: Random noisy input analysis for Dataset #4 (Prostate) at various noise level.

Methods	50		100		200	
	HD(mm)	CC	HD(mm)	CC	HD(mm)	CC
ISO-Surface	36.49 (6.28)	43.40 (4.94)	38.34 (6.18)	83.9 (8.48)	39.85 (6.61)	165.4 (15.6)
NVR-Poisson ^{1,2}	3.01 (0.88)	1.08 (0.39)	3.79 (4.07)	1.23 (0.44)	\	\
Neural-Pull ²	29.23 (5.47)	723 (2368)	28.14 (5.38)	48.2 (17.4)	32.48 (5.68)	3056 (4440)
FUNSR(Ours) ²	2.73 (3.98)	1.08 (0.40)	2.98 (5.19)	1.08 (0.39)	4.12 (7.87)	1.15 (0.59)
FUNSR-PE ³	2.44 (3.43)	1.06 (0.30)	2.76 (4.29)	1.04 (0.20)	3.28 (5.61)	1.15 (0.75)

¹ Only second stage of *NVR-Poisson* is involved since Dataset #4 already contains reconstructed 3D volume.

² *NVR-Poisson* fails to fit the convex hull at noise level 200 and the batch size of *Neural-Pull* and *FUNSR* are set to 10000 at this noise level.

³ Reconstruction performance of *FUNSR* with additional Positional Encoding (PE).

bifurcations are forcibly closed in Dataset# 3 (CAB) and small raised tumors in Dataset #4 (Prostate) are erased. Additionally, *Neural-Pull* lacks integrity across all datasets due to the absence of geometric constraints. Overall, our method demonstrates superior performance in both fidelity and visualization.

We further evaluate the smoothness of reconstructed meshes from different methods using Dataset #2. Fig. 4 shows the descriptive statistics (mean and interquartile range) of Gaussian curvature computation and associated kernel density estimation (KDE) on the normalized, reconstructed mesh of each carotid artery shape. Top plots show the variation of Gaussian curvature across different

radii. We then choose a stable radius of 0.0195 and the other two radii 0.0045 and 0.0255 for density estimation at the bottom plots. In comparison to other three methods, *FUNSR (Ours)* shows superior ability in predicting more continuous and smooth surfaces without resolution limitations. This is evidenced by the maximal probability and minimal variation in the interquartile range.

5.2. Various input analysis

As previously noted, *ISO-Surface* exhibits the poorest performance on Dataset #1 (phantom) due to unexpected noise and outliers introduced by simple threshold segmentation. In this section, we conduct three experiments to

explore the sensitivity of different surface reconstruction methods to different categories of input noise, including automatic segmentation input, various random noise levels and motion perturbations.

5.2.1. Automatic segmentation input

Firstly, we utilize the automatic segmentation (Auto-Seg) masks of Dataset #3 (CAB)-test as input to assess the performance of different methods. Fig. 5 summarizes the results both quantitatively and qualitatively. The boxplots clearly show that our method can partially filter out abnormal segmentation caused by network, achieving the lowest HD compared to other methods. Specifically, FUNSR exhibits a 21% reduction in HD compared to the original Auto-Seg results. The 3D visualization presented on the right of Fig. 5 aligns with boxplots, indicating our method’s efficacy in handling anomalies in detailed 3D structures. Furthermore, 2D section visually illustrates the enhanced resolution achieved by our method.

5.2.2. Random noise levels

We then experiment the performance of different methods under various noise levels by introducing random outliers around the mask in volume space using Dataset #4 (prostate). Three noise levels are introduced: 50, 100 and 200. Two evaluation metrics that showed significant variance, HD and CC, are reported in Table 2. Unsurprisingly, ISO-Surface has the worst results, as its reconstruction directly reflects the entire structure of input. The second stage of NVR-Poisson method displays competitive performance against noise interference (Kazhdan et al., 2006), since Poisson reconstruction method typically tends to produce a closed shape. However, this method fails to reconstruct mesh at a high noise level, e.g., 200. The HD and CC of our method, with an original batch size of 5000 at this noise level, are 6.07 ± 10.17 mm and 1.38 ± 1.49 , respectively. While these two metrics are improved to 4.12 ± 7.87 mm and 1.15 ± 0.59 when batch size is increased to 10,000. Moreover, HD and CC can be further decreased across all three noise levels by incorporating additional positional encoding (PE) (Zheng et al., 2023; Tancik et al., 2020).

Fig. 6 visually presents two examples with respect to the reconstructed meshes at three noise levels: 50, 100 and 200. ISO-Surface method retains all input geometric information, resulting in reconstructed meshes containing

all random outliers, as indicated by gray boxes. NVR-Poisson tends to over-smooth surface details and cannot fit the proper convex hull at noise level of 200 for these two cases. Both our method and our method with PE demonstrate superiority in addressing random noisy inputs, as highlighted by red boxes. On the right of Fig. 6, we show a failure case of our method at noise level of 200, where the network is unable to correctly restore clear shape under such high-level noise. However, positional encoding can aid our network in fully reconstructing the actual prostate structure.

5.2.3. Motion perturbation

We further analyze the influence of random perturbation on transducer’s motion during freehand scan using Dataset #2 (CCA). We separately perturb the rotation component ($\mathbf{R} \in SO(3)$) and translation component ($\mathbf{t} \in \mathbb{R}^3$) of each pose with additive noise \mathbf{n}_r and \mathbf{n}_t following Esposito et al. (2019) and Chen et al. (2023b). Here, \mathbf{n}_r and \mathbf{n}_t are elements of $\mathfrak{se}(3)$ Lie algebra, with $\mathbf{n}_r \sim \mathcal{N}(\mathbf{0}, \sigma_r \mathbf{I})$ and $\mathbf{n}_t \sim \mathcal{N}(\mathbf{0}, \sigma_t \mathbf{I})$. The motion perturbation is represented in 6-DOF (degree-of-freedom) and formulated as $\mathbf{T} = [\mathbf{R} | \mathbf{t}] \in SE(3)$. Here, $SO(3)$ and $SE(3)$ stand for the Special Orthogonal (SO) group and Special Euclidean (SE) group in three dimensions, respectively.

Fig. 7(a) demonstrates the performance degradation of four methods under various motion perturbations ranging from 0 (no perturbation) to $[\sigma_r = 5e - 2, \sigma_t = 1e - 1]$, which corresponds to a maximum absolute deviation of 9.86 degrees in rotation and 0.32 pixels in translation. It is evident that ISO-Surface is highly susceptible to interference from motion, as shown by HD plot and visual comparison in Fig. 7(b). The fragments and holes in the reconstructed mesh from NVR-Poisson method lead to a serious decrease in DSC starting at $[\sigma_r = 6e - 3, \sigma_t = 2e - 2]$, and yielding the worst DSC and HD at level $[\sigma_r = 5e - 2, \sigma_t = 1e - 1]$. To plot this level, we exclude the cases where the convex hull cannot be fit for mesh generation. Consistent with previous experiments, Neural-Pull losses complete shape contour across all input categories. Our proposed FUNSR presents competitive reconstruction quality compared to other three methods and shows ability to handle the largest level of perturbation at $[\sigma_r = 1e - 2, \sigma_t = 5e - 2]$. The value of HD eventually increases to a similar discrepancy as ISO-Surface and Neural-Pull at $[\sigma_r = 5e - 2, \sigma_t = 1e - 1]$. Fig. 7(b) qual-

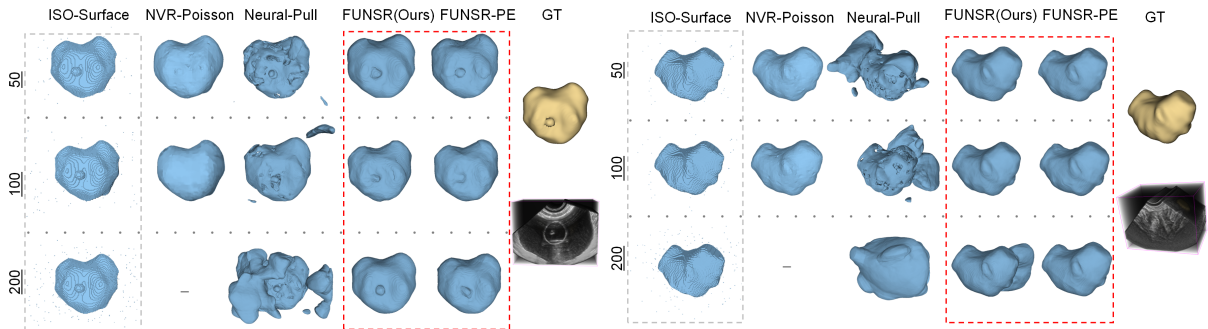


Figure 6: Visual comparisons of random noisy input analysis for Dataset #4 (prostate) at noise level 50, 100 and 200. All the random outliers reconstructed by ISO-Surface are bounded by gray boxes. Our method (FUNSR) and our method with positional encoding (FUNSR-PE) are in red boxes. Ground truth (GT) label and volume space are presented at the top and bottom for reference.

itatively shows three typical perturbation levels as well as corresponding reconstructed meshes from four methods. The comparisons highlight our advantage of noise robustness.

5.3. Computation cost analysis

Differing from ISO-Surface, which directly reconstructs the mesh from segmented mask, other three methods involve downsampling operation for the network input. In this section, therefore, we explore the impact of downsampling size on reconstruction performance and computation cost using Dataset #2 (CCA). The results are plotted in Fig. 7 (c). The time required for NVR-Poisson method shows no variation across different downsampling sizes, with an average duration of 182.3 minutes. This suggests that the computational cost for this method is primarily driven by training of semantic-NVR. Although the proposed geometric constraints introduced a slight computational burden than Neural-Pull, the total processing time is still within the accepted range, about 3.5 minutes. Besides, Fig. 7 (c) indicates that 20,000 points can achieve a balance between performance and time for our method under the current setting of query point generation.

Additionally, we investigated the performance of Neural-Pull and our method at different numbers of training iterations, as well as the computational time. Fig. 7 (d) shows the unstable convergence of Neural-Pull at different iteration steps, in contrast to consistent performance exhibited by our approach. Meanwhile, the plots reveal that training for 1.5×10^4 steps of our method achieves a

balance between the reconstructed quality and time cost. Moreover, a considerable performance can be rapidly produced at 5000 iterations, which takes less than 1 minute. The above results significantly demonstrate the ability of our method to realize high reconstruction quality and fast convergence speed.

5.4. Ablation Study

In this subsection, to investigate the capability of each module in proposed method, we perform a comprehensive ablation study on Dataset #1 (phantoms), which has CAD model as ground truth. The experiments include exploring the effectiveness of two geometric constraints and performance of point cloud modalities. We train the network for 2.0×10^4 iterations and compare the results of each module at 1.5×10^4 and 2.0×10^4 iterations. Neural-Pull is chosen as the baseline method.

5.4.1. Validating the effectiveness of geometric constraints

The effectiveness of our method is attributed to the incorporation of two geometric constraints, SCC and OSC-ADL. We have individually evaluated their efficiency on two hip phantom models through both qualitative and quantitative analysis. The ablation study is carried out by separately adding SCC and OSC-ADL to the baseline.

Table 3 reports individual contribution of SCC and OSC-ADL to the enhancement of surface reconstruction performance. Compared with baseline at 1.5×10^4 iterations, the SCC results improve by 54% for CD and 33%

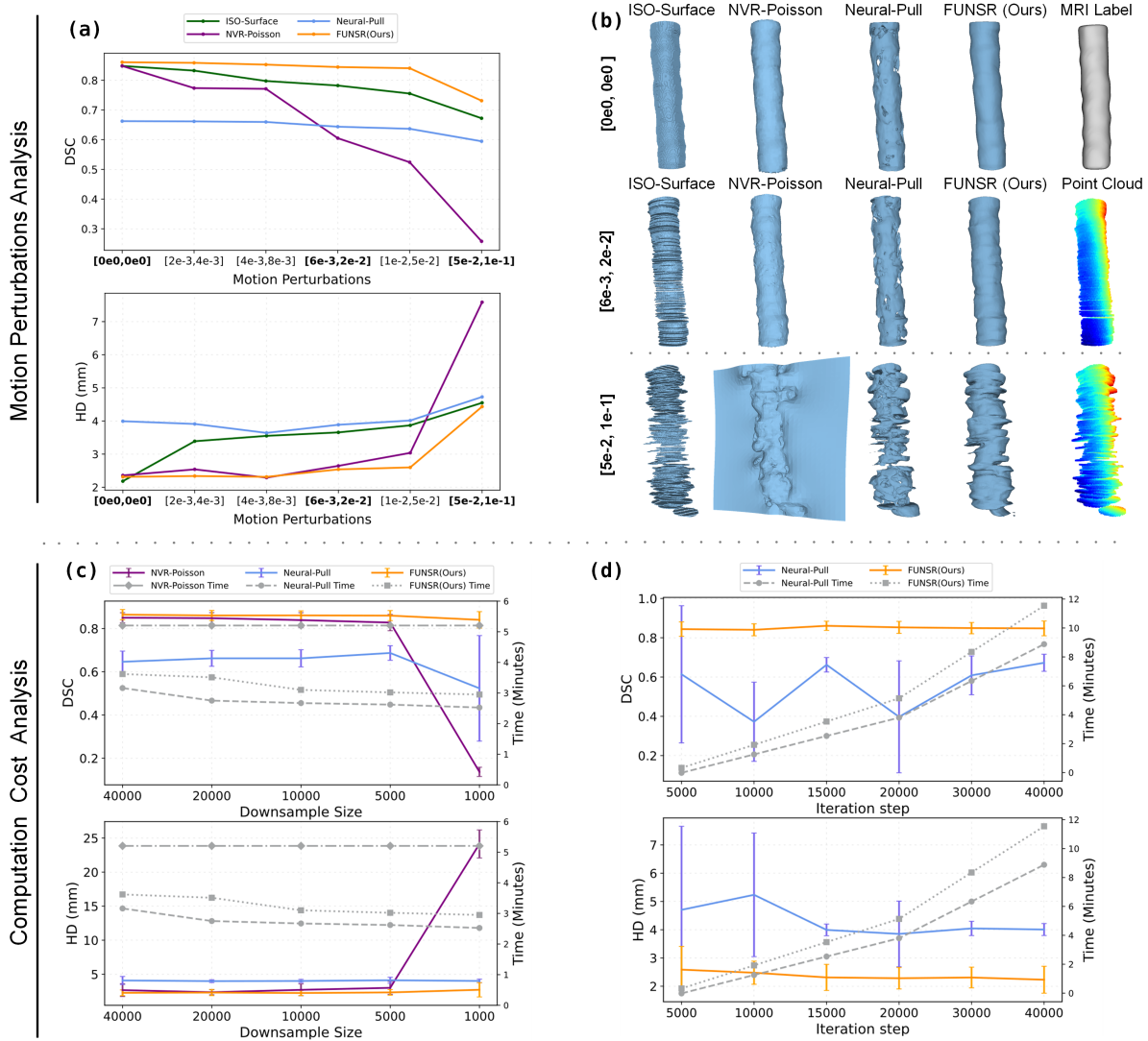


Figure 7: Quantitative and qualitative analysis of motion perturbation and computation cost for Dataset #2 (CCA). (a) Plots of Dice Similarity Coefficient (DSC) and Hausdorff Distance (HD) across four methods under six perturbation levels. (b) Visualization of reconstructed meshes from four methods under three typical perturbation levels: $[\sigma_r = 0e0, \sigma_t = 0e0]$ (no motion perturbation), $[\sigma_r = 6e-3, \sigma_t = 2e-2]$, and $[\sigma_r = 5e-2, \sigma_t = 1e-1]$. MRI label and perturbed point clouds are shown for reference. (c) Computation cost of various downsampling sizes for NVR-Poisson, Neural-Pull and FUNSR (Ours) at 1.5×10^4 iterations. The time for NVR-Poisson is presented on a logarithmic scale. (d) Computation cost of different training iteration steps for Neural-Pull and FUNSR (Ours) with a downsampling size of 20,000.

Table 3: Ablation studies on the effectiveness of geometric constraints using Dataset #1 (phantoms) at 1.5×10^4 and 2.0×10^4 iterations.

Module	1.5×10^4		2.0×10^4	
	CD (mm)	HD (mm)	CD (mm)	HD (mm)
Baseline	2.78(0.36)	3.43(2.02)	3.29(0.38)	4.21(1.44)
+SCC	1.26(0.09)	2.31(1.57)	1.29(0.16)	2.34(0.95)
+OSC-ADL	1.67(0.11)	2.67(1.39)	1.75(0.54)	2.65(0.84)
FUNSR(Ours)	1.04 (0.01)	2.09(1.59)	1.23(0.15)	1.97(1.01)

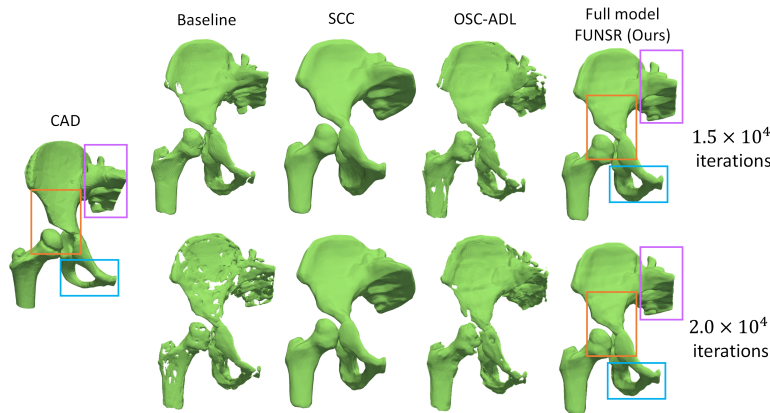


Figure 8: Visualization of the ablation study on the H1 phantom in Dataset #1 for validation of geometric constraints. The top and bottom plots are reconstructed surfaces of baseline (Neural-pull), only SCC, only OSC-ADL and full model (FUNSR) at 1.5×10^4 and 2.0×10^4 iterations, respectively. The CAD model is shown on the left. Three colored boxes highlight the prominent differences.

for HD. OSC-ADL also demonstrates a decrease of 40% for CD and 22% for HD. Furthermore, the most significant improvements are observed when both constraints are jointly optimized in proposed method, revealing a lower CD (63%) and HD (39%) on two phantoms. Our method can also improve the accuracy by decreasing 63% CD, 53% HD at 2.0×10^4 .

Fig. 8 shows an example of ablation study conducted on H1 phantom model. Baseline method presents the worst structures, showing the broken surface and imperfect shape due to unstable training, especially at 2.0×10^4 iterations. SCC constraint illustrates the ability to reconstruct overall shape at both iterations compared to the baseline. However, only using SCC fails to handle certain tough detailed structures at 1.5×10^4 iterations, as indicated by the purple and blue boxes. The edge of the sacrum (purple) appears to be inflated and obturator fora-

men at the bottom (blue) is filled. In contrast, OSC-ADL module can recover the detailed structures, but lose the completeness of general morphology due to the absence of SCC. By combining both constraints, our proposed method is able to effectively preserve all the structures.

5.4.2. Comparing the appearance of the VPC with SPC

In this experiment, we investigate our network performance using surface point cloud (SPC) or volumetric point cloud (VPC) as input. The SPC data, which serves as the original input for baseline, is extracted only from segmented boundary. While the VPC data is generated from all the voxels within segmentation masks. A visual contrastive analysis of two input modalities is shown on the right of Fig. 9. The VPC exhibits a dense aggregation of 3D points within the mask area, which provides enriched information for underlying shape representation.

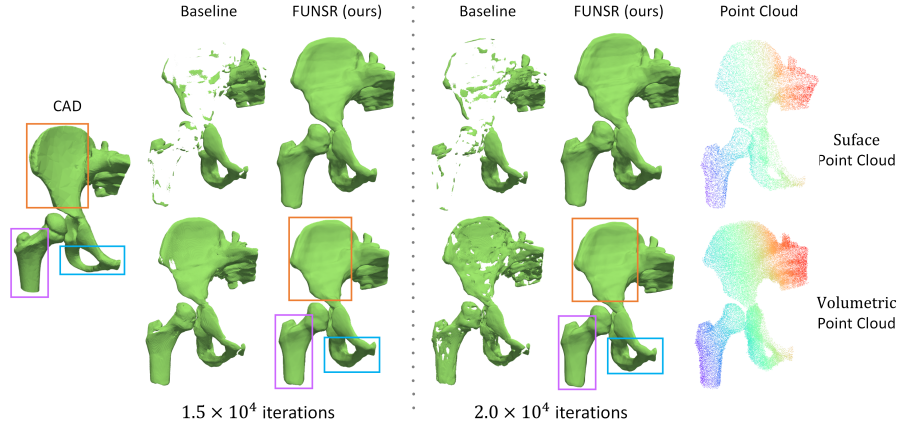


Figure 9: Visualization of the ablation study on the H1 phantom in Dataset #1 for comparison of different inputs. The results at 1.5×10^4 and 2.0×10^4 iterations are presented on the left block and right block. The top and bottom plots are reconstructed surface of baseline (Neural-pull) and our method using surface point cloud and volumetric point cloud, respectively. The CAD model is shown on the left. Blue-to-red color in point cloud indicates the directional changes from left to right. Three colored boxes highlight the prominent differences.

Table 4: Ablation studies on the performance of two input point cloud modalities, surface point cloud (S) versus volumetric point cloud (V), using Dataset #1 (Phantom) at 1.5×10^4 and 2.0×10^4 iterations.

Methods	1.5×10^4		2.0×10^4	
	CD (mm)	HD (mm)	CD (mm)	HD (mm)
Baseline-S	12.35(2.39)	24.20(1.52)	13.26(1.06)	23.78(2.34)
Baseline-V	2.78(0.36)	3.43(2.02)	3.29(0.38)	4.21(1.44)
Proposed-S	1.12(0.06)	2.17(1.58)	1.43(0.41)	2.07(0.92)
Proposed-V	1.04(0.01)	2.09(1.59)	1.23(0.15)	1.97(1.01)

Therefore, only using SPC as input will lead the network to produce a coarser local surface or even lose integrity as opposed to the results using VPC. Main differences are most apparent on the three highlight boxes. Our method shows the advantage of representing continuity and completeness, particularly in achieving a smoother surface when using VPC, as indicated by the orange and blue boxes in Fig. 9.

We also present a quantitative assessment using CD and HD in Table 4. The numerical results align with visual inspection in Fig. 9, with baseline showing that SPC input yields the highest CD and HD due to the vanishing boundaries in reconstructed mesh. In contrast, the performance of our method utilizing SPC or VPC is both significantly improved in comparison to baseline and achieves the low-

est discrepancy when using VPC.

6. Discussion and Conclusion

We propose FUNSR, an end-to-end self-supervised surface reconstruction model designed to tackle the challenges in 3D freehand US, including the limited resolution and noise-segmented boundary for representation of anatomical structure. Although the proposed method proves to be valuable for the current situation, it's important to acknowledge limitations and discuss future work to address them. First, even though the reconstruction time for individual subject is already 3.5 minutes by using a single NVIDIA RTX 3090 GPU, the computational efficiency can still be improved for possible real-time reconstruction (Kerbl et al., 2023). For simplicity, we directly

consider the entire segmentation mask as volumetric input in this study. Future studies could benefit from investigating resampling strategies that concentrate on sampling more points around the boundary and fewer points at the center of the mask to accelerate reconstruction process further. Second, the input of VPC will result in a pseudo-SDF field inside the shape. While the primary goal of this paper is to accurately reconstruct surface structure and simultaneously generate an external signed distance field for possible navigation applications, a more precise internal distance field and inner structure could be achieved with assistance of multi-view US scans or unsigned distance functions (Chen et al., 2023a).

In summary, we have developed a novel DL-based approach that incorporates geometric constraints to learn SDFs of neural implicit surface reconstruction for free-hand 3D US volume. The proposed constraints allow us to effectively minimize the sign variations and reconstruction errors during the training. The results demonstrate our method is highly effective at reconstructing the 3D surface of medical anatomical structures. Additionally, we show that our approach can be directly applied to 3D US volumes for surface reconstruction. The promising results have the potential to advance applications of 3D US in medical augmented reality, surgical navigation, and computer-assisted interventions.

Appendix A.

Table A1 summarizes the datasets and detailed technical parameters of used data acquisition systems. The spacing size of voxel grid is set according to the pixel size of US transducer based on previous works (Chen et al., 2020; Li et al., 2023; Zhang et al., 2023; Baum et al., 2023).

Acknowledgement

This research was supported by the Natural Science Foundation of China (NSFC) under Grant No.12074258 and a grant from Natural Science Foundation of China (NSFC) under Grant No.62071299, and a grant from Alberta Innovates - Accelerating Innovations into CarE (AICE) program under Grant No. RES0056222.

CRediT authorship contribution statement

Hongbo Chen: Writing - Original Draft, Conceptualization (Equal), Methodology (Equal), Visualization, Software. **Logiraj Kumaralingam:** Writing - Review & Editing, Conceptualization (Equal), Methodology (Equal), Validation (Equal). **Shuhang Zhang:** Visualization, Validation. **Sheng Song:** Data Curation, Software. **Fayi Zhang:** Resources, Software. **Haibin Zhang:** Resources, Data Curation. **Thanh-Tu Pham:** Data Curation. **Kumaradevan Punithakumar:** Writing - Review & Editing. **Edmond H. M. Lou:** Investigation, Data Curation. **Yuyao Zhang:** Data Curation, Funding Acquisition. **Lawrence H. Le:** Writing - Review & Editing, Funding Acquisition. **Rui Zheng:** Writing - Review & Editing, Funding Acquisition, Supervision.

References

- Amiranashvili, T., Lüdke, D., Li, H.B., Zachow, S., Menze, B.H., 2024. Learning continuous shape priors from sparse data with neural implicit functions. *Medical Image Analysis* 94, 103099. doi:10.1016/j.media.2024.103099.
- Atzmon, M., Lipman, Y., 2020. SAL: Sign Agnostic Learning of Shapes From Raw Data, in: 2020 IEEE/CVF Conference on Computer Vision and Pattern Recognition (CVPR), pp. 2562–2571. doi:10.1109/CVPR42600.2020.00264.
- Baorui, M., Zhizhong, H., Yu-Shen, L., Matthias, Z., 2021. Neural-pull: Learning signed distance functions from point clouds by learning to pull space onto surfaces, in: International Conference on Machine Learning (ICML).
- Battle, V.M., Montiel, J.M.M., Fua, P., Tardós, J.D., 2023. LightNeuS: Neural Surface Reconstruction in Endoscopy Using Illumination Decline, in: Greenspan, H., Madabhushi, A., Mousavi, P., Salcudean, S., Duncan, J., Syeda-Mahmood, T., Taylor, R. (Eds.), *Medical Image Computing and Computer Assisted Intervention – MICCAI 2023*, Springer Nature Switzerland, Cham. pp. 502–512. doi:10.1007/978-3-031-43999-5_48.

Table A1: Appendix A: Overview of datasets, data acquisition systems, grid size and data segmentation methods in the experiments.

Data	Sweep	Ultrasound Transducer	Frequency	Tracking Device	Grid Size	Segment
#1	2	Clarius, C3HD Canada	5 MHz	Polhemus G4, U.S.A.	0.5 (mm)	Threshold
#2	10	Clarius, L7HD Canada	10 MHz	Polhemus G4, U.S.A.	0.2 (mm)	Manual Labeling
#3	77	Clarius, L7HD Canada	10 MHz	Polhemus G4, U.S.A.	0.2 (mm)	Network & Manual Labeling
#4	73	Clinic TRUS Machine	9 MHz	-	0.8 (mm)	Organizer

* Grid size is set following (Chen et al., 2020; Li et al., 2023; Zhang et al., 2023; Baum et al., 2023) for Dataset #1, Dataset #2, Dataset #3 and Dataset #4, respectively.

- Baum, Z.M.C., Saeed, S.U., Min, Z., Hu, Y., Barratt, D.C., 2023. MR to Ultrasound Registration for Prostate Challenge - Dataset, in: Medical Image Computing and Computer Assisted Intervention – MICCAI 2023. Zenodo, Zenodo. doi:10.5281/zenodo.7870105.
- Bongratz, F., Rickmann, A.M., Wachinger, C., 2024. Neural deformation fields for template-based reconstruction of cortical surfaces from MRI. Medical Image Analysis 93, 103093. doi:10.1016/j.media.2024.103093.
- Chen, H., Kumaralingam, L., Li, J., Punithakumar, K., Le, L.H., Zheng, R., 2023a. Neural Implicit Representation for Three-dimensional Ultrasound Carotid Surface Reconstruction using Unsigned Distance Function, in: 2023 IEEE International Ultrasonics Symposium (IUS), pp. 1–3. doi:10.1109/IUS51837.2023.10307668.
- Chen, H., Zheng, R., Lou, E., Le, L.H., 2020. Compact and Wireless Freehand 3D Ultrasound Real-time Spine Imaging System: A pilot study, in: 2020 42nd Annual International Conference of the IEEE Engineering in Medicine Biology Society (EMBC), pp. 2105–2108. doi:10.1109/EMBC44109.2020.9176614.
- Chen, H.B., Zheng, R., Qian, L.Y., Liu, F.Y., Song, S., Zeng, H.Y., 2021. Improvement of 3-D Ultrasound Spine Imaging Technique Using Fast Reconstruction Algorithm. IEEE Transactions on Ultrasonics, Ferroelectrics, and Frequency Control 68, 3104–3113. doi:10.1109/TUFFC.2021.3087712.
- Chen, Y., Chen, X., Wang, X., Zhang, Q., Guo, Y., Shan, Y., Wang, F., 2023b. Local-to-Global Registration for Bundle-Adjusting Neural Radiance Fields, in: 2023 IEEE/CVF Conference on Computer Vision and Pattern Recognition (CVPR), IEEE, Vancouver, BC, Canada. pp. 8264–8273. doi:10.1109/CVPR52729.2023.00799.
- Chou, G., Chugunov, I., Heide, F., 2022. Gensdf: Two-stage learning of generalizable signed distance functions, in: Proc. of Neural Information Processing Systems (NeurIPS).
- Cruz, R.S., Lebrat, L., Bourgeat, P., Fookes, C., Fripp, J., Salvado, O., 2021. DeepCSR: A 3D Deep Learning Approach for Cortical Surface Reconstruction, in: 2021 IEEE Winter Conference on Applications of Computer Vision (WACV), pp. 806–815. doi:10.1109/WACV48630.2021.00085.
- Driess, D., Ha, J.S., Toussaint, M., Tedrake, R., 2021. Learning Models as Functionals of Signed-Distance Fields for Manipulation Planning, in: 5th Annual Conference on Robot Learning.
- Eid, M.C., Yeung, P.H., Wyburd, M.K., Henriques, J.F., Namburete, A.I.L., 2024. RapidVol: Rapid Recon-

- struction of 3D Ultrasound Volumes from Sensorless 2D Scans, arXiv. doi:[10.48550/arXiv.2404.10766](https://doi.org/10.48550/arXiv.2404.10766), [arXiv:2404.10766](https://arxiv.org/abs/2404.10766).
- Esposito, M., Hennersperger, C., Göbl, R., Demaret, L., Storath, M., Navab, N., Baust, M., Weinmann, A., 2019. Total Variation Regularization of Pose Signals With an Application to 3D Freehand Ultrasound. *IEEE Transactions on Medical Imaging* 38, 2245–2258. doi:[10.1109/TMI.2019.2898480](https://doi.org/10.1109/TMI.2019.2898480).
- Farshian, A., Götz, M., Cavallaro, G., Debus, C., Nießner, M., Benediktsson, J.A., Streit, A., 2023. Deep-Learning-Based 3-D Surface Reconstruction—A Survey. *Proceedings of the IEEE* 111, 1464–1501. doi:[10.1109/JPROC.2023.3321433](https://doi.org/10.1109/JPROC.2023.3321433).
- Gaits, F., Mellado, N., Basarab, A., 2024. Ultrasound volume reconstruction from 2D Freehand acquisitions using neural implicit representations, in: 21st IEEE International Symposium on Biomedical Imaging (ISBI 2024), IEEE Signal Processing Society and IEEE Engineering in Medicine and Biology Society, Athènes, Greece. p. à paraître.
- Gopinath, K., Desrosiers, C., Lombaert, H., 2021. SegRecon: Learning Joint Brain Surface Reconstruction and Segmentation from Images, in: de Bruijne, M., Cattin, P.C., Cotin, S., Padoy, N., Speidel, S., Zheng, Y., Essert, C. (Eds.), *Medical Image Computing and Computer Assisted Intervention – MICCAI 2021*, Springer International Publishing, Cham. pp. 650–659. doi:[10.1007/978-3-030-87234-2_61](https://doi.org/10.1007/978-3-030-87234-2_61).
- Guo, H., Chao, H., Xu, S., Wood, B.J., Wang, J., Yan, P., 2022. Ultrasound Volume Reconstruction From Freehand Scans Without Tracking. *IEEE Transactions on Biomedical Engineering* , 1–11 doi:[10.1109/TBME.2022.3206596](https://doi.org/10.1109/TBME.2022.3206596).
- Huang, Q., Zeng, Z., 2017. A Review on Real-Time 3D Ultrasound Imaging Technology. *BioMed Research International* 2017, 1–20. doi:[10.1155/2017/6027029](https://doi.org/10.1155/2017/6027029).
- Jiang, M., Chiu, B., 2023. A dual-stream centerline-guided network for segmentation of the common and internal carotid arteries from 3D ultrasound images. *IEEE Transactions on Medical Imaging* , 1–11 doi:[10.1109/TMI.2023.3263537](https://doi.org/10.1109/TMI.2023.3263537).
- Kazhdan, M., Bolitho, M., Hoppe, H., 2006. Poisson surface reconstruction, in: *Proceedings of the fourth Eurographics symposium on Geometry processing*.
- Kerbl, B., Kopanas, G., Leimkuehler, T., Drettakis, G., 2023. 3D Gaussian Splatting for Real-Time Radiance Field Rendering. *ACM Transactions on Graphics* 42, 139:1–139:14. doi:[10.1145/3592433](https://doi.org/10.1145/3592433).
- Kerr, W., Rowe, P., Pierce, S.G., 2017. Accurate 3D reconstruction of bony surfaces using ultrasonic synthetic aperture techniques for robotic knee arthroplasty. *Computerized Medical Imaging and Graphics* 58, 23–32. doi:[10.1016/j.compmedig.2017.03.002](https://doi.org/10.1016/j.compmedig.2017.03.002).
- Laumer, F., Amrani, M., Manduchi, L., Beuret, A., Rubi, L., Dubatovka, A., Matter, C.M., Buhmann, J.M., 2023. Weakly supervised inference of personalized heart meshes based on echocardiography videos. *Medical Image Analysis* 83, 102653. doi:[10.1016/j.media.2022.102653](https://doi.org/10.1016/j.media.2022.102653).
- Li, H., Chen, H., Jing, W., Li, Y., Zheng, R., 2021. 3D Ultrasound Spine Imaging with Application of Neural Radiance Field Method, in: *2021 IEEE International Ultrasonics Symposium (IUS)*, pp. 1–4. doi:[10.1109/IUS52206.2021.9593917](https://doi.org/10.1109/IUS52206.2021.9593917).
- Li, J., Huang, Y., Song, S., Chen, H., Shi, J., Xu, D., Zhang, H., Chen, M., Zheng, R., 2023. Automatic Diagnosis of Carotid Atherosclerosis Using a Portable Freehand 3D Ultrasound Imaging System. doi:[10.48550/arXiv.2301.03081](https://doi.org/10.48550/arXiv.2301.03081), [arXiv:2301.03081](https://arxiv.org/abs/2301.03081).
- Li, R., Li, X., Fu, C.W., Cohen-Or, D., Heng, P.A., 2019. Pu-gan: a point cloud upsampling adversarial network, in: *IEEE International Conference on Computer Vision (ICCV)*.
- Liu, S., Wang, Y., Yang, X., Lei, B., Liu, L., Li, S.X., Ni, D., Wang, T., 2019. Deep Learning in Medical Ultrasound Analysis: A Review. *Engineering* 5, 261–275. doi:[10.1016/j.eng.2018.11.020](https://doi.org/10.1016/j.eng.2018.11.020).
- Lorensen, W.E., Cline, H.E., 1987. Marching cubes: A high resolution 3D surface construction algorithm. *ACM SIGGRAPH Computer Graphics* 21, 163–169. doi:[10.1145/37402.37422](https://doi.org/10.1145/37402.37422).

- Luo, M., Yang, X., Wang, H., Dou, H., Hu, X., Huang, Y., Ravikumar, N., Xu, S., Zhang, Y., Xiong, Y., Xue, W., Frangi, A.F., Ni, D., Sun, L., 2023. RecON: On-line learning for sensorless freehand 3D ultrasound reconstruction. *Medical Image Analysis* 87, 102810. doi:[10.1016/j.media.2023.102810](https://doi.org/10.1016/j.media.2023.102810).
- Luo, M., Yang, X., Wang, H., Du, L., Ni, D., 2022. Deep Motion Network for Freehand 3D Ultrasound Reconstruction, in: Wang, L., Dou, Q., Fletcher, P.T., Speidel, S., Li, S. (Eds.), *Medical Image Computing and Computer Assisted Intervention – MICCAI 2022*, Springer Nature Switzerland, Cham. pp. 290–299. doi:[10.1007/978-3-031-16440-8_28](https://doi.org/10.1007/978-3-031-16440-8_28).
- Ma, Q., Li, L., Robinson, E.C., Kainz, B., Rueckert, D., Alansary, A., 2023. CortexODE: Learning Cortical Surface Reconstruction by Neural ODEs. *IEEE Transactions on Medical Imaging* 42, 430–443. doi:[10.1109/TMI.2022.3206221](https://doi.org/10.1109/TMI.2022.3206221).
- Mao, X., Li, Q., Xie, H., Lau, R.Y., Wang, Z., Paul Smolley, S., 2017. Least squares generative adversarial networks, in: *Proceedings of the IEEE International Conference on Computer Vision (ICCV)*.
- Martelli, B., 2022. An Introduction to Geometric Topology, arXiv. [arXiv:1610.02592](https://arxiv.org/abs/1610.02592).
- Meng, Q., Bai, W., O'Regan, D.P., Rueckert, D., 2024. DeepMesh: Mesh-Based Cardiac Motion Tracking Using Deep Learning. *IEEE Transactions on Medical Imaging* 43, 1489–1500. doi:[10.1109/TMI.2023.3340118](https://doi.org/10.1109/TMI.2023.3340118).
- Mescheder, L., Oechsle, M., Niemeyer, M., Nowozin, S., Geiger, A., 2019. Occupancy Networks: Learning 3D Reconstruction in Function Space, in: *Proceedings of the IEEE/CVF Conference on Computer Vision and Pattern Recognition*, pp. 4460–4470.
- Mildenhall, B., Srinivasan, P.P., Tancik, M., Barron, J.T., Ramamoorthi, R., Ng, R., 2020. Nerf: Representing scenes as neural radiance fields for view synthesis, in: *ECCV*.
- Mohamed, F., Siang, C.V., 2019. A Survey on 3D Ultrasound Reconstruction Techniques. *IntechOpen*. doi:[10.5772/intechopen.81628](https://doi.org/10.5772/intechopen.81628).
- Molaei, A., Aminimehr, A., Tavakoli, A., Kazerouni, A., Azad, B., Azad, R., Merhof, D., 2023. Implicit Neural Representation in Medical Imaging: A Comparative Survey, in: *Proceedings of the IEEE/CVF International Conference on Computer Vision*, pp. 2381–2391.
- Mozaffari, M.H., Lee, W.S., 2017. Freehand 3-D Ultrasound Imaging: A Systematic Review. *Ultrasound in Medicine & Biology* 43, 2099–2124. doi:[10.1016/j.ultrasmedbio.2017.06.009](https://doi.org/10.1016/j.ultrasmedbio.2017.06.009).
- Nakao, M., Tong, F., Nakamura, M., Matsuda, T., 2021. Image-to-Graph Convolutional Network for Deformable Shape Reconstruction from a Single Projection Image, in: de Bruijne, M., Cattin, P.C., Cotin, S., Padoy, N., Speidel, S., Zheng, Y., Essert, C. (Eds.), *Medical Image Computing and Computer Assisted Intervention – MICCAI 2021*, Springer International Publishing, Cham. pp. 259–268. doi:[10.1007/978-3-030-87202-1_25](https://doi.org/10.1007/978-3-030-87202-1_25).
- Namburete, A.I.L., Papież, B.W., Fernandes, M., Wyburd, M.K., Hesse, L.S., Moser, F.A., Ismail, L.C., Gunier, R.B., Squier, W., Ohuma, E.O., Carvalho, M., Jaffer, Y., Gravett, M., Wu, Q., Lambert, A., Winsley, A., Restrepo-Méndez, M.C., Bertino, E., Purwar, M., Barros, F.C., Stein, A., Noble, J.A., Molnár, Z., Jenkinson, M., Bhutta, Z.A., Papageorghiou, A.T., Villar, J., Kennedy, S.H., 2023. Normative spatiotemporal fetal brain maturation with satisfactory development at 2 years. *Nature* 623, 106–114. doi:[10.1038/s41586-023-06630-3](https://doi.org/10.1038/s41586-023-06630-3).
- Nguyen, D.V., Vo, Q.N., Le, L.H., Lou, E.H.M., 2015. Validation of 3D surface reconstruction of vertebrae and spinal column using 3D ultrasound data – A pilot study. *Medical Engineering & Physics* 37, 239–244. doi:[10.1016/j.medengphy.2014.11.007](https://doi.org/10.1016/j.medengphy.2014.11.007).
- Park, J.J., Florence, P., Straub, J., Newcombe, R., Lovegrove, S., 2019. DeepSDF: Learning Continuous Signed Distance Functions for Shape Representation, in: *Proceedings of the IEEE/CVF Conference on Computer Vision and Pattern Recognition*, pp. 165–174.
- Popescu-Pampu, P., 2016. What Is the Genus?. volume 2162 of *Lecture Notes in Mathematics*. Springer

- International Publishing, Cham. doi:[10.1007/978-3-319-42312-8](https://doi.org/10.1007/978-3-319-42312-8).
- Prager, R.W., Ijaz, U.Z., Gee, A.H., Treece, G.M., 2010. Three-dimensional ultrasound imaging. *Proceedings of the Institution of Mechanical Engineers, Part H: Journal of Engineering in Medicine* 224, 193–223. doi:[10.1243/09544119JEIM586](https://doi.org/10.1243/09544119JEIM586).
- Prevost, R., Salehi, M., Jagoda, S., Kumar, N., Sprung, J., Ladikos, A., Bauer, R., Zettinig, O., Wein, W., 2018. 3D freehand ultrasound without external tracking using deep learning. *Medical Image Analysis* 48, 187–202. doi:[10.1016/j.media.2018.06.003](https://doi.org/10.1016/j.media.2018.06.003).
- Reed, A., Kim, J., Blanford, T., Pediredla, A., Brown, D., Jayasuriya, S., 2023. Neural Volumetric Reconstruction for Coherent Synthetic Aperture Sonar. *ACM Transactions on Graphics* 42, 113:1–113:20. doi:[10.1145/3592141](https://doi.org/10.1145/3592141).
- Rohling, R., Gee, A., Berman, L., 1999. A comparison of freehand three-dimensional ultrasound reconstruction techniques. *Medical Image Analysis* 3, 339–359. doi:[10.1016/S1361-8415\(99\)80028-0](https://doi.org/10.1016/S1361-8415(99)80028-0).
- Sander, J., De Vos, B.D., Bruns, S., Planken, N., Viergever, M.A., Leiner, T., Išgum, I., 2023. Reconstruction and completion of high-resolution 3D cardiac shapes using anisotropic CMRI segmentations and continuous implicit neural representations. *Computers in Biology and Medicine* 164, 107266. doi:[10.1016/j.compbiomed.2023.107266](https://doi.org/10.1016/j.compbiomed.2023.107266).
- Santa Cruz, R., Lebrat, L., Fu, D., Bourgeat, P., Fripp, J., Fookes, C., Salvado, O., 2022. CorticalFlow⁺⁺: Boosting Cortical Surface Reconstruction Accuracy, Regularity, and Interoperability, in: Wang, L., Dou, Q., Fletcher, P.T., Speidel, S., Li, S. (Eds.), *Medical Image Computing and Computer Assisted Intervention – MICCAI 2022*, Springer Nature Switzerland, Cham. pp. 496–505. doi:[10.1007/978-3-031-16443-9_48](https://doi.org/10.1007/978-3-031-16443-9_48).
- Song, B., Shen, L., Xing, L., 2023. PINER: Prior-Informed Implicit Neural Representation Learning for Test-Time Adaptation in Sparse-View CT Reconstruction, in: *Proceedings of the IEEE/CVF Winter Conference on Applications of Computer Vision*, pp. 1928–1938.
- Song, S., Huang, Y., Li, J., Chen, M., Zheng, R., 2022. Development of implicit representation method for freehand 3d ultrasound image reconstruction of carotid vessel, in: *2022 IEEE International Ultrasonics Symposium (IUS)*, pp. 1–4. doi:[10.1109/IUS54386.2022.9958448](https://doi.org/10.1109/IUS54386.2022.9958448).
- Tancik, M., Srinivasan, P.P., Mildenhall, B., Fridovich-Keil, S., Raghavan, N., Singhal, U., Ramamoorthi, R., Barron, J.T., Ng, R., 2020. Fourier Features Let Networks Learn High Frequency Functions in Low Dimensional Domains, arXiv. doi:[10.48550/arXiv.2006.10739](https://doi.org/10.48550/arXiv.2006.10739), arXiv:2006.10739.
- Treece, G., Prager, R., Gee, A., 1999. Regularised marching tetrahedra: Improved iso-surface extraction. *Computers & Graphics* 23, 583–598. doi:[10.1016/S0097-8493\(99\)00076-X](https://doi.org/10.1016/S0097-8493(99)00076-X).
- Velikova, Y., Azampour, M.F., Simson, W., Esposito, M., Navab, N., 2024. Implicit Neural Representations for Breathing-compensated Volume Reconstruction in Robotic Ultrasound, arXiv. doi:[10.48550/arXiv.2311.04999](https://doi.org/10.48550/arXiv.2311.04999), arXiv:2311.04999.
- Wang, Z., Nakao, M., Nakamura, M., Matsuda, T., 2021. Shape Reconstruction for Abdominal Organs based on a Graph Convolutional Network. *2021 43rd Annual International Conference of the IEEE Engineering in Medicine & Biology Society (EMBC)*, 2960–2963doi:[10.1109/EMBC46164.2021.9630826](https://doi.org/10.1109/EMBC46164.2021.9630826).
- Wickramasinghe, U., Remelli, E., Knott, G., Fua, P., 2020. Voxel2Mesh: 3D Mesh Model Generation from Volumetric Data, in: Martel, A.L., Abolmaesumi, P., Stoyanov, D., Mateus, D., Zuluaga, M.A., Zhou, S.K., Racoceanu, D., Joskowicz, L. (Eds.), *Medical Image Computing and Computer Assisted Intervention – MICCAI 2020*, Springer International Publishing, Cham. pp. 299–308. doi:[10.1007/978-3-030-59719-1_30](https://doi.org/10.1007/978-3-030-59719-1_30).
- Wiesner, D., Suk, J., Dummer, S., Nečasová, T., Ulman, V., Svoboda, D., Wolterink, J.M., 2024. Generative

- modeling of living cells with SO(3)-equivariant implicit neural representations. *Medical Image Analysis* 91, 102991. doi:[10.1016/j.media.2023.102991](https://doi.org/10.1016/j.media.2023.102991).
- Wysocki, M., Azampour, M.F., Eilers, C., Busam, B., Salehi, M., Navab, N., 2023. Ultra-NeRF: Neural Radiance Fields for Ultrasound Imaging, in: *Medical Imaging with Deep Learning*.
- Xu, J., Moyer, D., Gagoski, B., Iglesias, J.E., Grant, P.E., Golland, P., Adalsteinsson, E., 2023. NeSVoR: Implicit Neural Representation for Slice-to-Volume Reconstruction in MRI. *IEEE Transactions on Medical Imaging* 42, 1707–1719. doi:[10.1109/TMI.2023.3236216](https://doi.org/10.1109/TMI.2023.3236216).
- Yeung, P.H., Aliasi, M., Papageorgiou, A.T., Haak, M., Xie, W., Namburete, A.I., 2021. Learning to map 2D ultrasound images into 3D space with minimal human annotation. *Medical Image Analysis* 70, 101998. doi:[10.1016/j.media.2021.101998](https://doi.org/10.1016/j.media.2021.101998).
- Yeung, P.H., Hesse, L.S., Aliasi, M., Haak, M.C., Xie, W., Namburete, A.I.L., 2024. Sensorless volumetric reconstruction of fetal brain freehand ultrasound scans with deep implicit representation. *Medical Image Analysis* 94, 103147. doi:[10.1016/j.media.2024.103147](https://doi.org/10.1016/j.media.2024.103147).
- Zha, R., Cheng, X., Li, H., Harandi, M., Ge, Z., 2023. EndoSurf: Neural Surface Reconstruction of Deformable Tissues with Stereo Endoscope Videos, in: Greenspan, H., Madabhushi, A., Mousavi, P., Salcudean, S., Duncan, J., Syeda-Mahmood, T., Taylor, R. (Eds.), *Medical Image Computing and Computer Assisted Intervention – MICCAI 2023*, Springer Nature Switzerland, Cham. pp. 13–23. doi:[10.1007/978-3-031-43996-4_2](https://doi.org/10.1007/978-3-031-43996-4_2).
- Zhang, F., Li, J., Huang, Y., Chen, M., Zheng, R., 2023. Investigation of Interactive Segmentation for Bifurcation of Carotid Artery on 3D Ultrasound Image Volume, in: *2023 IEEE International Ultrasonics Symposium (IUS)*, pp. 1–4. doi:[10.1109/IUS51837.2023.10306567](https://doi.org/10.1109/IUS51837.2023.10306567).
- Zhang, W.Y., Rohling, R.N., Pai, D.K., 2004. Surface extraction with a three-dimensional freehand ultrasound system. *Ultrasound in Medicine & Biology* 30, 1461–1473. doi:[10.1016/j.ultrasmedbio.2004.08.020](https://doi.org/10.1016/j.ultrasmedbio.2004.08.020).
- Zhang, Y., Rohling, R., Pai, D., 2002. Direct surface extraction from 3D freehand ultrasound images, in: *IEEE Visualization, 2002. VIS 2002.*, pp. 45–52. doi:[10.1109/VISUAL.2002.1183755](https://doi.org/10.1109/VISUAL.2002.1183755).
- Zhao, F., Wang, W., Liao, S., Shao, L., 2021. Learning Anchored Unsigned Distance Functions With Gradient Direction Alignment for Single-View Garment Reconstruction, in: *Proceedings of the IEEE/CVF International Conference on Computer Vision*, pp. 12674–12683.
- Zheng, J., Li, X., Ramasinghe, S., Lucey, S., 2023. Robust Point Cloud Processing through Positional Embedding, arXiv. doi:[10.48550/arXiv.2309.00339](https://doi.org/10.48550/arXiv.2309.00339), [arXiv:2309.00339](https://arxiv.org/abs/2309.00339).
- Zhou, H., Jagadeesan, J., 2020. Real-Time Dense Reconstruction of Tissue Surface From Stereo Optical Video. *IEEE Transactions on Medical Imaging* 39, 400–412. doi:[10.1109/TMI.2019.2927436](https://doi.org/10.1109/TMI.2019.2927436).